

# Three-dimensional flow dynamics and mixing in a gas-centered liquid-swirl coaxial injector at supercritical pressure F

Cite as: Phys. Fluids **31**, 065109 (2019); <https://doi.org/10.1063/1.5097163>

Submitted: 22 March 2019 . Accepted: 25 May 2019 . Published Online: 18 June 2019

Xingjian Wang , Yanxing Wang, and Vigor Yang 

## COLLECTIONS

F This paper was selected as Featured



View Online



Export Citation



CrossMark

## ARTICLES YOU MAY BE INTERESTED IN

[Deformation characteristics and energy conversion during droplet impact on a water surface](#)

Physics of Fluids **31**, 062108 (2019); <https://doi.org/10.1063/1.5099228>

[Three-dimensional numerical simulation of bubble rising in viscous liquids: A conservative phase-field lattice-Boltzmann study](#)

Physics of Fluids **31**, 063106 (2019); <https://doi.org/10.1063/1.5096390>

[Large-eddy simulation of an open-channel flow bounded by a semi-dense rigid filamentous canopy: Scaling and flow structure](#)

Physics of Fluids **31**, 065108 (2019); <https://doi.org/10.1063/1.5095770>



CAPTURE WHAT'S POSSIBLE  
WITH OUR NEW PUBLISHING ACADEMY RESOURCES

Learn more 





# Three-dimensional flow dynamics and mixing in a gas-centered liquid-swirl coaxial injector at supercritical pressure

Cite as: Phys. Fluids 31, 065109 (2019); doi: 10.1063/1.5097163

Submitted: 22 March 2019 • Accepted: 25 May 2019 •

Published Online: 18 June 2019



Xingjian Wang,  Yanxing Wang, and Vigor Yang<sup>a)</sup> 

## AFFILIATIONS

School of Aerospace Engineering, Georgia Institute of Technology, Atlanta, Georgia 30332, USA

<sup>a)</sup>vigor.yang@aerospace.gatech.edu

## ABSTRACT

Three-dimensional flow dynamics and mixing in a gas-centered liquid-swirl coaxial injector at supercritical pressure is numerically studied using the large-eddy-simulation technique. In this class of injectors, typical of liquid-fueled propulsion engines, high-temperature gaseous oxygen (GOX) is axially delivered into the center tube and kerosene is tangentially injected through discrete orifices into the coaxial annulus. The operating conditions and geometry mimic those of the main injector elements used in staged-combustion propulsion engines. The present work details the full three-dimensional flow evolution over the entire injector configuration, including axial and circumferential dynamics that are essential for small-scale mixing between GOX and kerosene. Various key flow structures and instability mechanisms in the injector, including axial and azimuthal shear-layer instabilities, secondary instabilities (baroclinic torque and volume dilatation), centrifugal instability, flow recirculation, and acoustic motion, are identified. The significance of these instability mechanisms is explored in the context of streamwise and azimuthal vorticity transport. The GOX core is found to exhibit a hexagonal shape, mainly due to the interactions of vortex rings detached from the center post and coaxial annulus. For comparison, a cylindrical sector of the configuration is also simulated. The results of the present study will support the design and development of high-performance injectors for future propulsion applications.

Published under license by AIP Publishing. <https://doi.org/10.1063/1.5097163>

## I. INTRODUCTION

This paper investigates three-dimensional flow dynamics and mixing in a gas-centered liquid-swirl coaxial (GCLSC) injector at supercritical pressure, where the environment pressure exceeds the thermodynamic critical points of the working fluids. The physical model mimics the injectors of the main combustion chambers of staged-combustion liquid rocket engines, such as the NK-33, RD-20, and RD-170/180 engines.<sup>1-5</sup> Figure 1 shows schematics of a GCLSC injector. High-temperature gaseous oxygen (GOX) from the preburner is axially delivered into the center tube (known as the GOX post), while liquid fuel is tangentially introduced into the coaxial annulus through discrete orifices uniformly distributed along the perimeter of the annulus. Mixing of the injected propellants takes place in the recess ( $L_1 \leq x \leq L_2$ ) and taper ( $L_2 \leq x \leq L_3$ ) regions. With such a relatively simple design, GCLSC injectors provide excellent combustion efficiency and

stability and have been extensively used in various propulsion devices for decades.

Significant progress has been made in the study of the mixing and combustion characteristics of GCLSC injectors. Experimental diagnostics<sup>6-10</sup> and numerical simulations<sup>11-13</sup> have been conducted over a broad range of geometric and operating conditions. Emphasis has been placed on the effects of recess length and gas-to-liquid momentum flux ratio on liquid atomization and stability behaviors. For example, Yang *et al.*<sup>6</sup> identified three different types of flow patterns that result from varying the recess length and developed a criterion for optimizing the recess length for liquid atomization. Their work provided direct insight into injector flow physics and can be effectively used for design optimization. Experimental studies on GCLSC injectors have generally been conducted at low or moderate pressure, while numerical studies<sup>12,13</sup> could reach the supercritical pressure level, the typical operating condition in liquid-propellant rocket engines. A brief summary of

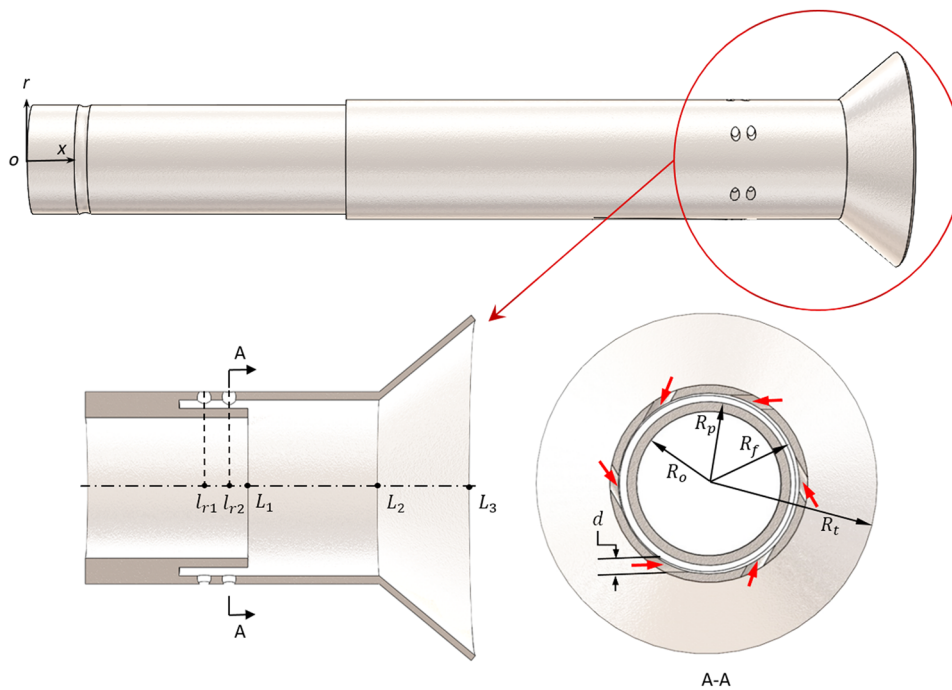


FIG. 1. Topical and cross-sectional views of a gas-centered liquid-swirl coaxial (GCLSC) injector.

the latest developments in numerical work in this area was given by Zhang *et al.*<sup>12</sup>

In spite of the efforts made to date, a full understanding of the key mechanisms of injector flow dynamics in a GCLSC injector remains elusive, especially the details of flow evolution in a three-dimensional configuration under high-pressure conditions. Figure 2 shows a snapshot of the density field at supercritical pressure, illustrating the dominant flow structures and instability mechanisms in a typical GCLSC injector. Eight different types of dynamics are identified, including recirculating flows in the wake of the GOX post rim and in the taper region (① and ⑤), due to the local geometric variation and swirl-induced centrifugal force. Atomization of the liquid film along the injection surface is achieved by shear-layer instabilities in both the axial and azimuthal directions (② and ⑥) and further enhanced by secondary instabilities through baroclinic and volume-dilatational effects (⑦). Each flow regime is characterized by its intrinsic time and length scales, and the regimes interact with each other. The purpose of the present work is to provide a comprehensive survey of the details of the flow structures within the injector and the near field downstream of the injector, with special attention to the spatiotemporal evolution of the flow instabilities that dictate the injector dynamics, as sketched in Fig. 2.

Experimental efforts have been made, over the last two decades, to study injector flow and combustion dynamics.<sup>14–19</sup> High-pressure conditions, however, impose severe limitations on experimental work, especially for optical diagnostics. The harsh environment makes it a formidable task to manage optical access to the combustion region, where, for example, special windows must be used to withstand the high-power lasers required for Raman diagnostics. Limited quantitative information (photographic images, shadow-graph visualizations, and OH\* emission data) has been obtained but

at considerable expense. Balance *et al.*<sup>10</sup> recently performed high-speed optical diagnostics on a GCLSC injector by means of side-on chemiluminescence and infrared images. GOX and liquid kerosene (RP-2) were used as propellants. Data were obtained in the pressure range of 2.0–16.5 MPa and the mixture-ratio range of 2.9–20.0. A borescope was used to image the flame from a location upstream of the GOX post, enabling visualization of the flame in its stabilization region. Their work provided much useful information, for the first time, at a scale sufficient to observe flame stabilization and the associated flow evolution at supercritical pressure.

Numerical studies on the supercritical fluid dynamics of GCLSC injectors have been performed using the large-eddy-simulation (LES) technique.<sup>12,13,20</sup> Only a section of the injector (along the azimuthal direction) was simulated in these studies, and such simplification introduces several limitations. First, the individual orifices for kerosene fuel injection are collectively treated as a slit along the radial boundary of the annulus. The behaviors of each individual fuel stream and the ensuing effect on the flow evolution are not considered. Second, flow variations in the circumferential direction, which are important for small-scale mixing, are neglected. Third, vortex stretching/tilting and other vorticity production mechanisms are ignored. While studies based on a sector configuration are capable of exploring many salient features of flow and combustion dynamics over a wide range of geometric parameters and operating conditions, a full three-dimensional investigation is needed to explore the complete flow evolution and dynamic characteristics, including vorticity dynamics and azimuthal instabilities. This motivates the present work.

This paper presents a full three-dimensional numerical study of supercritical fluid dynamics and mixing in a GCLSC injector, as shown schematically in Fig. 1. For comparison, a simple-sector

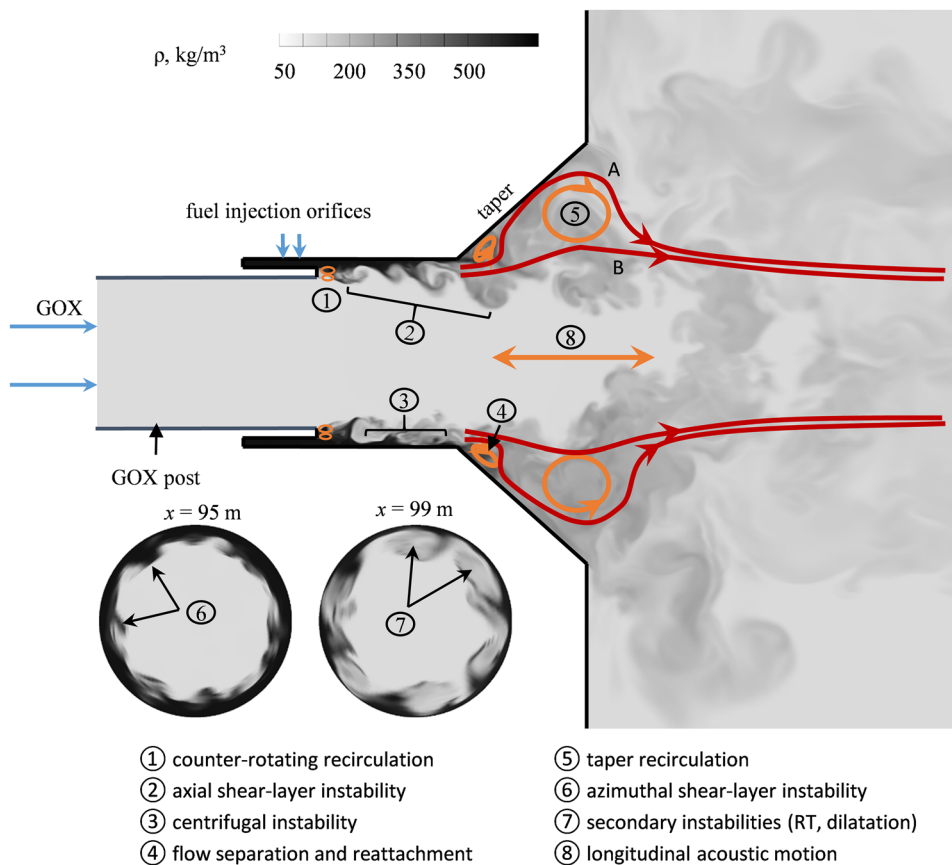


FIG. 2. Snapshot of density field illustrating key flow structures and instability mechanisms in a GCLSC injector.

simulation is also performed. The paper is organized as follows. Section II summarizes the theoretical formulation and numerical method for treating supercritical fluid flows. Section III describes the injector configuration and operating conditions. Section IV presents the results and detailed discussion. Finally, Sec. V draws conclusions.

## II. THEORETICAL AND NUMERICAL INFORMATION

The theoretical foundation of the present study is well documented in Refs. 21–23, which deal with supercritical fluid flows and combustion over the entire range of fluid thermodynamic states. Turbulence closure is achieved using the large-eddy-simulation (LES) technique, in which large-scale turbulent eddies are numerically resolved and small, subgrid-scale motions are modeled. A compressible version of the Smagorinsky model is employed to characterize the effects of subgrid-scale motion. Thermodynamic properties, including density, enthalpy, and specific heat at constant pressure, are evaluated according to fundamental thermodynamics theories and a modified Soave-Redlich-Kwong equation of state.<sup>24</sup> Transport properties, including thermal conductivity and dynamic viscosity, are estimated using extended corresponding-state principles. Mass diffusivity is obtained by the Takahashi method calibrated for high-pressure conditions. The evaluation of

thermodynamic and transport properties has been validated and implemented in previous studies.<sup>21</sup>

There are many numerical challenges in solving supercritical fluid flows. For example, thermodynamic nonidealities and transport anomalies take place as the fluid transits from subcritical to supercritical conditions. Treating these abnormal changes in a manner consistent with the intrinsic characteristics of the numerical algorithm presents a major obstacle. In addition, the rapid variation of the fluid state and a wide range of length and time scales at high pressure pose the well-known stiffness problem. To this end, the numerical framework was established by implementing a preconditioning scheme and a unified treatment of general-fluid thermodynamics.<sup>25</sup> The framework employs a density-based, finite-volume methodology, along with a dual-time-step integration technique.<sup>26</sup> Temporal discretization is fulfilled using a second-order backward difference, and the inner-loop pseudotime term is integrated with a four-step Runge-Kutta scheme. Spatial discretization is obtained using a fourth-order central difference scheme in generalized coordinates. Fourth-order matrix dissipation is implemented to ensure numerical stability and minimum contamination of the solution.<sup>27</sup> Finally, a multiblock domain decomposition technique<sup>28</sup> associated with the message passing interface technique of parallel computing is applied to optimize computational speed.

TABLE I. Geometric parameters of the injector.

$d$ (mm)	$R_o$ (mm)	$R_p$ (mm)	$R_f$ (mm)	$R_t$ (mm)
1.10	5.62	6.36	7.03	15.7
$l_{r1}$ (mm)	$l_{r2}$ (mm)	$L_1$ (mm)	$L_2$ (mm)	$L_3$ (mm)
89.5	91.5	93.0	103.5	113.1

### III. INJECTOR CONFIGURATION AND BOUNDARY CONDITIONS

The GCLSC injector of concern consists of four regions: the center cylindrical tube (the GOX post), coaxial fuel annulus, recess region, and taper region, as shown schematically in Fig. 1. The latter two regions are referred to as the mixing cup, where the oxidizer/fuel mixing takes place. Liquid kerosene is tangentially introduced into the coaxial annulus through 12 circular holes in two rows. Table I lists the geometric parameters of the injector. The coordinate origin is located at the center of the entrance of the GOX post, which measures 5.62 mm in radius,  $R_o$ , 93.0 mm in length,  $L_1$ , and 0.74 mm in post thickness,  $h$  ( $=R_p - R_o$ ). The radii of the upper and lower annulus surface are  $R_f = 7.03$  mm and  $R_p = 6.36$  mm, respectively. The diameter of the fuel orifices is  $d = 1.10$  mm. The first row of fuel orifices is at an  $l_{r1}$  of 89.5 mm and the second row at an  $l_{r2}$  of 91.5 mm. The recess region ( $L_1 \leq x \leq L_2$ ) has been shown to have significant effects on the mixing and flame stabilization characteristics.<sup>12,13</sup> A recess length ( $L_2 - L_1$ ) of 10.5 mm was selected for the present configuration, in view of the trade-off between combustion efficiency and thermal protection. The injector exit is at an  $L_3$  of 113.1 mm with a radius,  $R_t$ , of 15.7 mm.

Table II lists the inflow boundary conditions. The ambient pressure ( $p_a$ ) is set to 25.3 MPa, substantially exceeding the thermodynamic critical points of both oxygen and kerosene. The Reynolds number,  $Re$ , is about  $2.50 \times 10^5$ , based on the GOX flow condition and post thickness. The mean injected velocities of the GOX and kerosene streams are 102 m/s and 65.3 m/s, respectively.

Both the full three-dimensional configuration and a simplified sector are considered in the present study. For the former case, the computational domain consists of the injector interior ( $20R_o$  in the axial direction) and a downstream region ( $30R_o$  and  $8R_o$  in the axial and radial directions, respectively). The discretized cell distributions for the GOX post, the recess and taper regions, and the region downstream of the injector are  $288 \times 128 \times 120$ ,  $320 \times 224 \times 120$ , and  $320 \times 320 \times 120$ , respectively. The total number of numerical cells is  $25.3 \times 10^6$ . The flow structures in the azimuthal direction are resolved by 120 cells. The cross section of each fuel injection orifice is filled with more than 40 surface cells to guarantee the

TABLE II. Inflow conditions.

	Oxidizer	Fuel
Fluid	GOX	Kerosene
Mass flow rate (kg/s)	1.33	0.477
Temperature (K)	688	492
Density (kg/m <sup>3</sup> )	131	641

conservation of flow properties. A grid convergence study was performed for the sector configuration in our previous work.<sup>12</sup> The grid resolution in axial and radial directions for the present full three-dimensional configuration is the same as the intermediate grid resolution (level 2) in Ref. 12 and 60 times higher in the azimuthal direction. An acoustically nonreflecting boundary condition<sup>29</sup> is implemented at the entrance of the GOX post. The downstream boundaries in both the axial and radial directions are treated by means of the method of characteristics<sup>30</sup> combined with the use of buffer zones.<sup>31</sup> No-slip and adiabatic boundary conditions are enforced at the injector surface. A reference pressure is applied to preserve the average pressure in the computational domain.

In the sector configuration, the assembly of injector orifices is simplified to a slit on the injector surface, as shown schematically in Fig. 3. The azimuthal span is  $5^\circ$ . Periodic boundary conditions are specified in the azimuthal direction. Such simplification leads to the exclusion of the vortex-stretching/tilting mechanisms responsible for turbulent energy transfer from large to small eddies, as well as azimuthal wave dynamics. To ensure dynamic similarity between the full and sector configurations, the width of the circular slit is deduced from the conservation laws. It is well established<sup>32</sup> that the geometric constant  $K$ , defined below, is the most important dimensionless parameter in determining dynamic similarity,

$$K = \frac{A_n R_{in}}{A_{in} R_n}, \tag{1}$$

where  $A_n$  and  $A_{in}$  are the cross-sectional areas of the fuel annulus and tangential inlet, respectively.  $R_n$  is the radius of the outer annulus surface, and  $R_{in}$  is the radius of the swirling arm, the distance from the axis of a tangential passage to the injector axis. The constant,  $K$ , analytically determines the characteristics of a swirl injector, including the flow coefficient, nozzle filling coefficient, and liquid-film spreading angle at the injector exit. For given values of  $R_{in}$ ,  $R_n$ ,  $A_n$ , and  $K$ , the cross-sectional area of the fuel inlet must be identical for the three-dimensional [ $A_{in,1} = 12\pi(d/2)^2$ ] and sector ( $A_{in,2} = 2\pi R_f \delta \cos \theta$ ) configurations. The slit width for the sector configuration thus becomes

$$\delta = \frac{3d^2}{2R_f \cos \theta}. \tag{2}$$

Here,  $d$  is the orifice diameter,  $\delta$  is the slit width, and  $\theta$  is the injection angle.

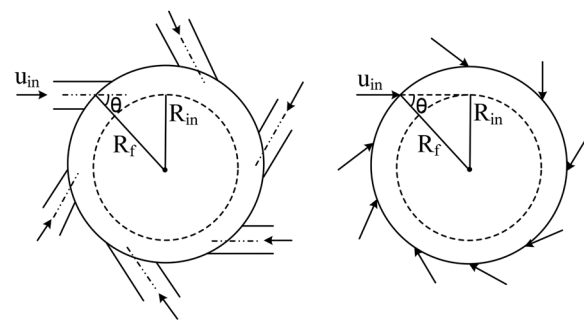


FIG. 3. Schematic of (left) discrete inlet orifices and (right) inlet slit.

#### IV. RESULTS AND DISCUSSION

Simulations were initiated by delivering GOX flow through the center tube of the injector. A velocity ramp was implemented to gradually increase the GOX inflow to the nominal condition while maintaining numerical stability. Liquid kerosene was then introduced into the coaxial annulus after the GOX flow had flushed out the initial transient in the computational domain. Data acquisition commenced when the flowfield reached its stationary state.

##### A. Instantaneous flowfield

Figure 4 shows typical snapshots of kerosene mass-fraction ( $y_F$ ) and vorticity-magnitude ( $|\omega| = |\nabla \times \mathbf{u}|$ ) fields for the full three-dimensional and sector configurations on the  $z = 0$  plane. Close similarities of main flow structures are observed. The kerosene stream forms a thin liquid film along the annulus surface. Mixing between GOX and kerosene begins in the recess region and intensifies in the taper region, mainly due to shear-layer instability and turbulent motions. Shear layers form along the surfaces of the GOX post and fuel annulus, separate from the wall, and develop into vortices, which convect downstream and grow into large billows. Further downstream, vortices merge in a pairing process. Amalgamation continues until the resultant vortex becomes so large as to break up and form small-scale structures.

Several unique flow features are identified for the full three-dimensional case. First, the GOX stream is enclosed by the mixing layer immediately downstream of the taper region, while it remains open in the sector configuration. Second, the kerosene film thickness decreases much faster in the full configuration, suggesting more efficient entrainment into and mixing with GOX. This can be attributed to the inclusion of complete vortical dynamics in the full three-dimensional case. Secondary small-scale instabilities occur because of the development of azimuthal waves and streamwise vortices. The fuel entrainment into the GOX stream is considerably stronger in the full configuration. Third, the difference between the flow structures in the upper and lower halves of the injector indicates flow nonuniformity in the circumferential direction. Azimuthal dynamics must be taken into account for accurate representation of the mixing process. Finally, the vortical field is more vigorous in the taper and downstream regions in the full configuration than in the sector configuration. The structures cover a wider range of scales, due to stretching and tilting, as well as other related mechanisms.

Figure 5 shows the isosurfaces of azimuthal velocity at values of  $-70$ ,  $-20$ , and  $10$  m/s (the upstream clockwise direction denotes the positive value). Inhomogeneous structures in the azimuthal direction are clearly observed. Discrete kerosene streams issuing from tangential orifices rotate counterclockwise into spiral structures with high azimuthal velocity amplitude (red isosurfaces). The velocity

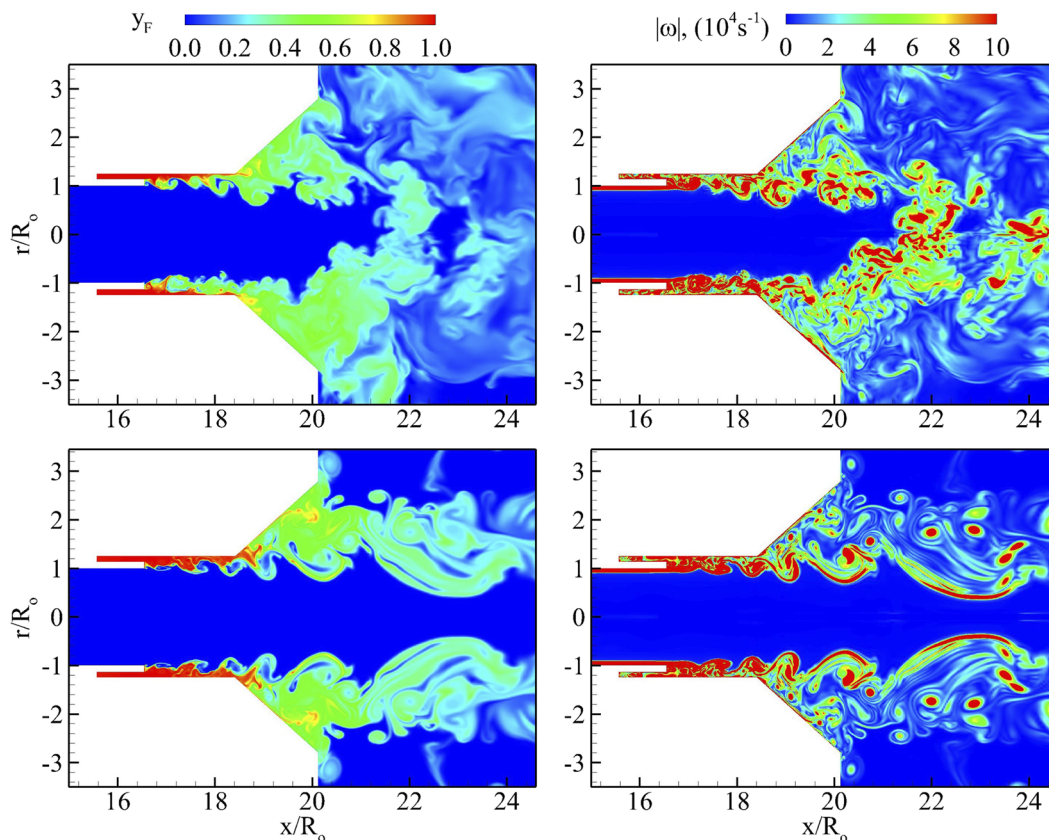
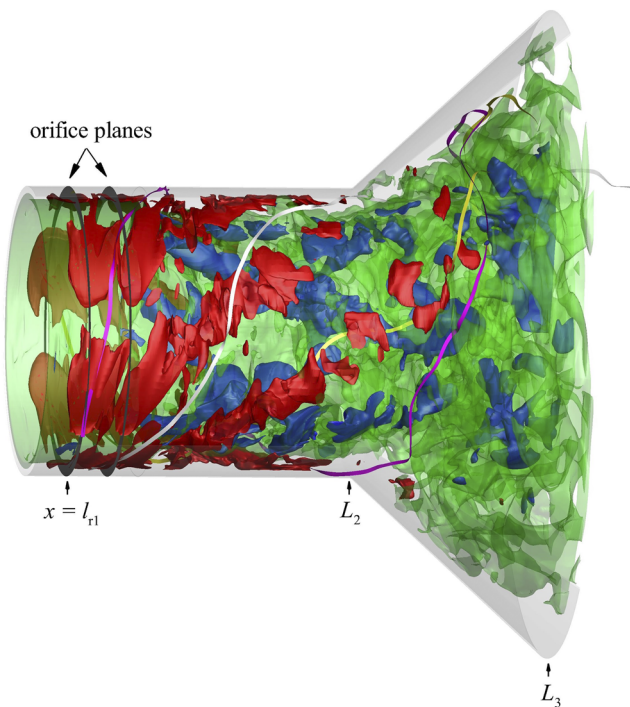


FIG. 4. Snapshots of kerosene mass fraction and vorticity magnitude fields on the  $z = 0$  plane for (top) full three-dimensional and (bottom) sector configurations.



**FIG. 5.** Isosurfaces of azimuthal velocity at values of  $-70$  (red),  $-20$  (green), and  $10$  (blue) m/s (ribbons denote streamlines issuing from the first row of orifices).

then decreases along the axial direction due to viscous dissipation and turbulent diffusion. The two streams in tandem from axially aligned orifices merge before the spiral structure forms. A total of six spiral structures form, corresponding to the six orifices on each injection plane. Clockwise rotation (blue isosurfaces) occurs on the GOX side of the mixing layer due to vortex roll up. This reversed flow pattern further promotes mixing and enhances circumferential inhomogeneity by introducing small-scale flow instabilities.

Figure 6 shows the isosurface of kerosene mass fraction at the value of 0.4, colored by azimuthal velocity distribution. The figure presents the azimuthally unwrapped view from the inside; the spiral structures appear as parallel streams. The lean angle of the aligned streams is determined by the ratio of the azimuthal to the axial velocity components. The isosurfaces are highly corrugated by hydrodynamic instabilities. The primary Kelvin-Helmholtz instability waves, induced by the axial and azimuthal velocity differences across shear layers, result in cone-shaped structures on each stream. The waves grow while traveling downstream and facilitate the entrainment of ambient fluids. The resultant vortices in the mixing layer are responsible for secondary instabilities in the transverse direction, which generate lobes and ligaments on the conical surface.

Two mechanisms are responsible for the formation of ligaments at the liquid surface: simple stretching of lobes and perforation of the sheared surface of lobes.<sup>33</sup> Surface tension plays an important role in the latter mechanism, which, however, diminishes in the present study of supercritical fluid flows. The mechanism of lobe stretching tends to dominate. Secondary instabilities, in particular, the Rayleigh-Taylor instability, are an important factor in

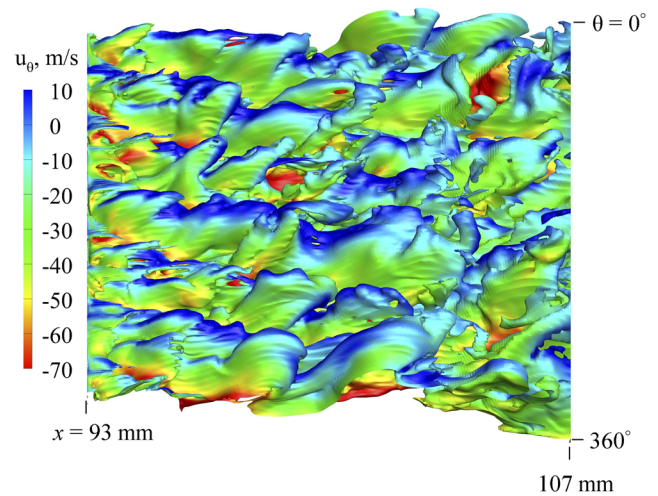


**FIG. 6.** Isosurface of kerosene mass fraction at 0.4, colored by azimuthal velocity and unwrapped in the azimuthal direction.

azimuthal dynamics. The Rayleigh-Taylor instability results from fluid acceleration at the liquid interface, which has been exposed to the primary Kelvin-Helmholtz shear instability. It can be viewed as a baroclinic effect due to the cross product of density and pressure gradients. Here, the pressure gradient is not related to gravitational acceleration but rather to the liquid acceleration caused by small-scale instabilities in the mixing region. Figure 7 shows the isosurface of the gauge pressure ( $p' = p - p_a$ ) at  $-5$  bars, overlaid by the pressure distribution on the wall of the fuel annulus, unwrapped in the azimuthal direction. The azimuthal instability is clearly observed from the formation of ligaments, highlighted by red circles in the

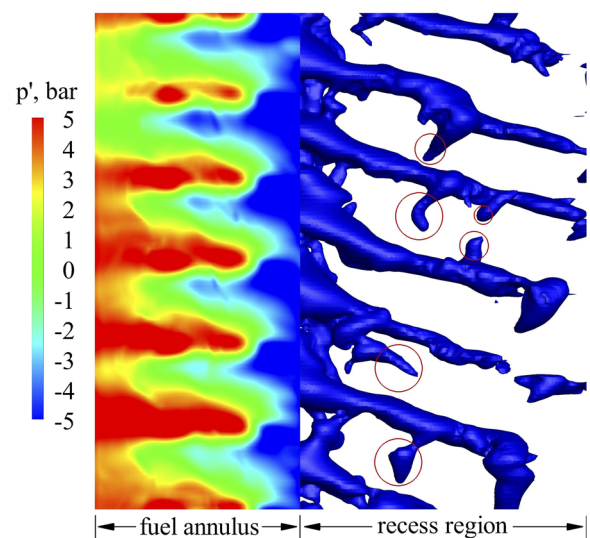


**FIG. 7.** Isosurface of gauge pressure at  $-5$  bars, overlaid by pressure surface distribution in the fuel annulus and unwrapped in the azimuthal direction.

recess region. As explained below, volume dilatation and baroclinic effects are substantial in this region and lead to significant vorticity production.

It is noteworthy that columnar low-pressure cores exist along fuel streams in Fig. 7. These cores result from local rotation of fluid parcels, as evidenced by the isosurfaces of azimuthal velocity in Fig. 8. Positive and negative velocity regions are intertwined with each other. The ensuing shear layers grow and roll up into vortices that are attached to the fuel streams. The strength of the vortices gradually decays, leading to the disappearance of the low-pressure cores at the exit of the recess region. In the fuel annulus, the gauge pressure is positive near the headend. It decreases continuously to negative values as the liquid fuel approaches the recess region. This negative zone is related to flow separation immediately downstream of the orifices.

Detailed flow dynamics are further examined on transverse cross sections. Figure 9 shows typical snapshots of gauge pressure, temperature, density, azimuthal velocity, vorticity magnitude, and kerosene mass fraction field at  $x = 97$  mm in the recess region. The gauge pressure near the surface varies periodically in the azimuthal direction. This pattern is caused by the centrifugal effect of bulk swirl of the fuel stream and local swirl of fluid parcels around the fuel stream. The bulk swirl enables a positive pressure gradient in the radial direction with a minimum value in the center, while the local swirl around the fuel stream leads to discrete low-pressure regions. The latter outweighs the former around the fuel stream, as indicated by negative pressure regions. Compared to the pressure and azimuthal velocity fields, the negative pressure regions reside between positive and negative azimuthal velocities and coincide with strong vortex cores.

The azimuthal shear layer along the liquid surface develops to wavy structures and vortices and subsequently leads to complex distributions of pressure and density, as indicated by the presence of lobes and ligaments. As a consequence, the pressure and density gradients are misaligned to form baroclinicity, which leads to the further production of vorticity. In addition, volume dilatation becomes evident, as shown by the corrugated distribution of temperature in

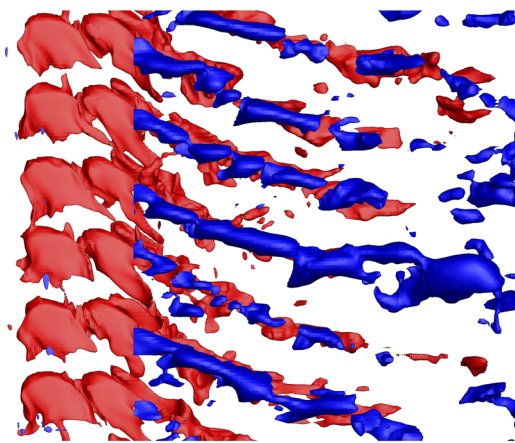


**FIG. 8.** Isosurfaces of azimuthal velocity (red:  $-70$  m/s; blue:  $10$  m/s), unwrapped in the azimuthal direction.

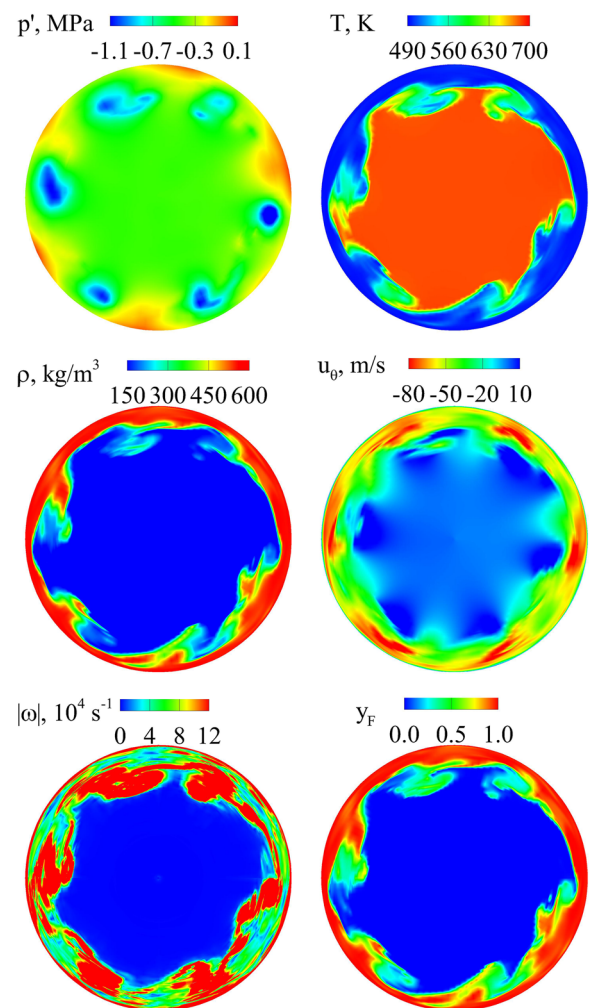


**FIG. 9.** Snapshots of gauge pressure, temperature, density, azimuthal velocity, vorticity magnitude, and kerosene mass fraction fields at  $x = 97$  mm in the recess region.

the vortex cores. The resultant vorticity field is very complex, and this facilitates propellant mixing. In the sector configuration (not shown), these mechanisms are not present because of the exclusion of azimuthal variation of flow properties. The calculated shear layer is sharper and results in less mixing in the vortex core, as indicated in Fig. 4. In short, in the full configuration, the primary azimuthal shear layer instability triggers secondary instabilities with baroclinic and dilatational effects. The ensuing vortical field significantly enhances the mixing of kerosene and GOX, as manifested by the green areas in the kerosene mass fraction field.

Figure 9 also reveals the circumferential nonuniformity of the liquid kerosene film. The film thickness varies periodically along the circumferential direction. The situation is related to the centrifugal instability driven by the circumferential change of azimuthal velocity. The swirl strength is proportional to the magnitude of azimuthal velocity. Higher magnitude implies stronger swirl and thus thinner

film. In regions of weaker swirl and thicker film, the liquid surface is perturbed by both shear-layer and secondary instabilities, leading to the formation of lobes and ligaments.

Figure 10 shows the spatially evolved kerosene mass fraction field along the axial direction in the recess and taper regions. It is overlaid by the six streamlines issuing from the first row of injection orifices. The streamlines are colored by kerosene mass fraction to trace the degree of mixing. The annular red region denotes the kerosene film, and the central blue region represents the GOX stream. Rather than smooth spiral structures, the streamlines are highly corrugated by local flow dynamics in the recess region. This lengthens flow residence time and offers more time for mixing. The kerosene film is nearly depleted before it enters the taper region. The GOX stream initially has a cylindrical shape and becomes irregular because of the Kelvin-Helmholtz and secondary instabilities. The former produces axisymmetric vortices in the azimuthal direction, while the latter generates finer structures. These instability mechanisms are further explored in terms of vorticity dynamics in Sec. IV B.

### B. Vorticity dynamics

Vorticity dynamics can be quantified using the following transport equation:<sup>34</sup>

$$\frac{D\boldsymbol{\omega}}{Dt} = (\boldsymbol{\omega} \cdot \nabla)\mathbf{u} - \boldsymbol{\omega}(\nabla \cdot \mathbf{u}) + \frac{1}{\rho^2} \nabla \rho \times \nabla p + \nabla \times \left( \frac{\nabla \times \boldsymbol{\tau}}{\rho} \right), \quad (3)$$

where  $\boldsymbol{\omega}$  and  $\mathbf{u}$  are the vorticity and velocity vectors, respectively, and  $\boldsymbol{\tau}$  is the viscous stress tensor. The left hand side is the substantial derivative of vorticity. The terms on the right hand side consist of vortex stretching/tilting, volume dilatation, baroclinic torque, and viscous diffusion. The vorticity budget in both the streamwise and azimuthal directions is discussed in the following. The contribution

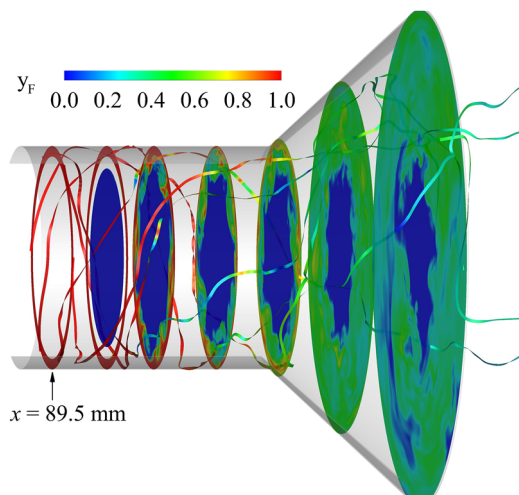


FIG. 10. Spatially evolved distributions of kerosene mass fraction at different axial locations in recess and taper regions, overlaid by streamlines originating from the first column of six injector orifices at  $x = 89.5$  mm and colored by kerosene mass fraction.

of viscous diffusion is assumed to be negligible in the flow regions of interest and is thus not considered here. The transport equations for streamwise and azimuthal vorticity components in cylindrical coordinates are expressed as

$$\frac{D\omega_x}{Dt} = (\boldsymbol{\omega} \cdot \nabla)u_x - \omega_x(\nabla \cdot \mathbf{u}) + \frac{1}{\rho^2} (\nabla \rho \times \nabla p)_x, \quad (4)$$

$$\frac{D\omega_\theta}{Dt} = (\boldsymbol{\omega} \cdot \nabla)u_\theta - \omega_\theta(\nabla \cdot \mathbf{u}) + \frac{1}{\rho^2} (\nabla \rho \times \nabla p)_\theta. \quad (5)$$

Given the gradient operator,  $\nabla = (\partial/\partial r; \partial/r\partial\theta; \partial/\partial x)$ , in the cylindrical coordinate system, Eqs. (4) and (5) are expanded and

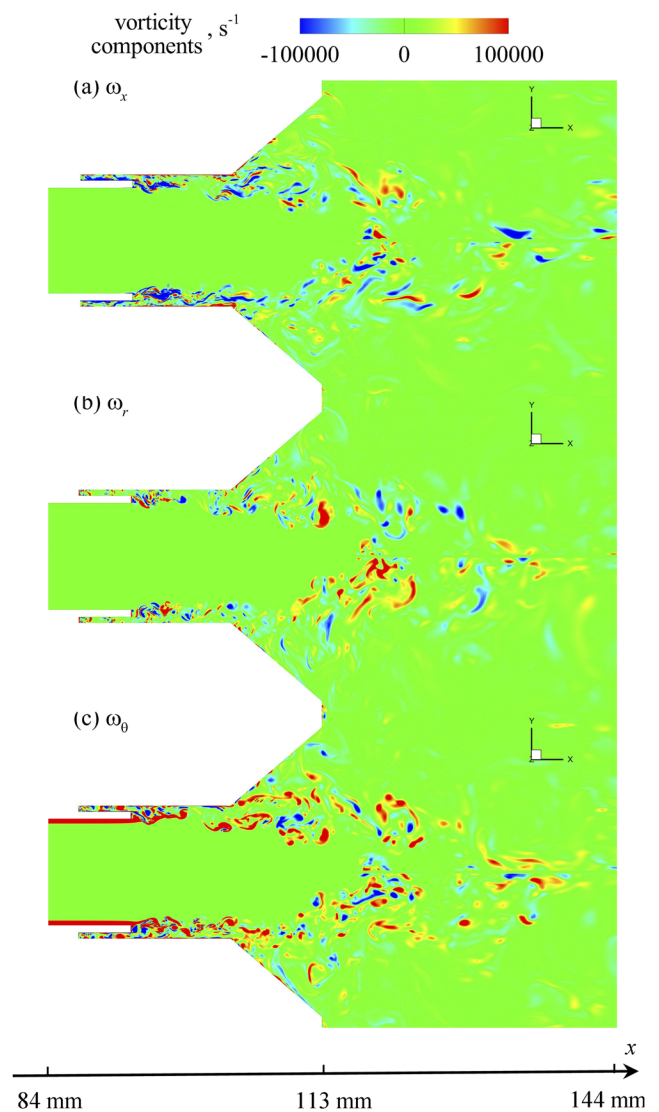


FIG. 11. Instantaneous distributions of vorticity components on the  $z = 0$  plane.

organized as follows:

$$\frac{D\omega_x}{Dt} = \left( \omega_r \frac{\partial u_x}{\partial r} + \frac{\omega_\theta}{r} \frac{\partial u_x}{\partial \theta} + \omega_x \frac{\partial u_x}{\partial x} \right) - \omega_x \left( \frac{1}{r} \frac{\partial r u_r}{\partial r} + \frac{1}{r} \frac{\partial u_\theta}{\partial \theta} + \frac{\partial u_x}{\partial x} \right) + \frac{1}{r\rho^2} \left( \frac{\partial \rho}{\partial \theta} \frac{\partial p}{\partial r} - \frac{\partial \rho}{\partial r} \frac{\partial p}{\partial \theta} \right), \tag{6}$$

$$\frac{D\omega_\theta}{Dt} = \left( \omega_r \frac{\partial u_\theta}{\partial r} + \frac{\omega_\theta}{r} \frac{\partial u_\theta}{\partial \theta} + \omega_x \frac{\partial u_\theta}{\partial x} \right) - \omega_\theta \left( \frac{1}{r} \frac{\partial r u_r}{\partial r} + \frac{1}{r} \frac{\partial u_\theta}{\partial \theta} + \frac{\partial u_x}{\partial x} \right) + \frac{1}{\rho^2} \left( \frac{\partial \rho}{\partial r} \frac{\partial p}{\partial x} - \frac{\partial \rho}{\partial x} \frac{\partial p}{\partial r} \right), \tag{7}$$

where  $r$ ,  $\theta$ , and  $x$  denote coordinate indices in the radial, azimuthal, and streamwise directions, respectively.

Figure 11 shows instantaneous distributions of vorticity components on the  $z = 0$  plane. The azimuthal vorticity ( $\omega_\theta = \partial u_r/\partial x - \partial u_x/\partial r$ ) prevails, and this is mainly attributed to the dominance of the axial velocity gradient in the radial direction. The axial velocity decreases across the shear layer with the increasing radial position, causing positive azimuthal vorticity to dominate throughout the flowfield. Negative azimuthal vorticity appears in the taper and downstream regions due to the radial expansion of the flow as shown in Fig. 12. Negative values occur when the decreasing rate of radial velocity in the axial direction overrides its axial velocity counterpart in the radial direction. A previous study has shown that the generation of negative azimuthal vorticity is an essential feature of vortex breakdown.<sup>35</sup> In the present work, generation of negative azimuthal vorticity is related to local flow recirculation near the taper exit. The radial expansion in the taper region reduces the centrifugal force ( $\partial p/\partial r \sim u_\theta^2/r$ ) and subsequently the radial pressure gradient. As a result, an adverse pressure gradient arises in the axial direction and leads to flow reversal at various local spots.

Figure 13 shows snapshots of the production of azimuthal vorticity, including vortex stretching and tilting, volume dilatation, and baroclinic torque calculated based on Eq. (7). Vortex stretching and tilting dominate vorticity production throughout the flowfield, though the other two mechanisms are non-negligible. Volume dilatational and baroclinic effects are substantial in the wake of the GOX post tip, where the mixing begins with fluids of different temperatures and species constituents. The corresponding

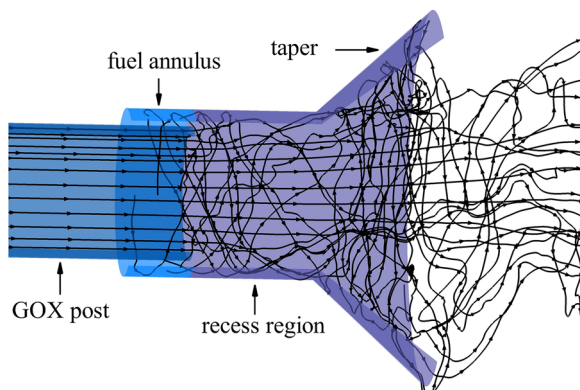


FIG. 12. Instantaneous streamlines issuing from the GOX post and fuel annulus.

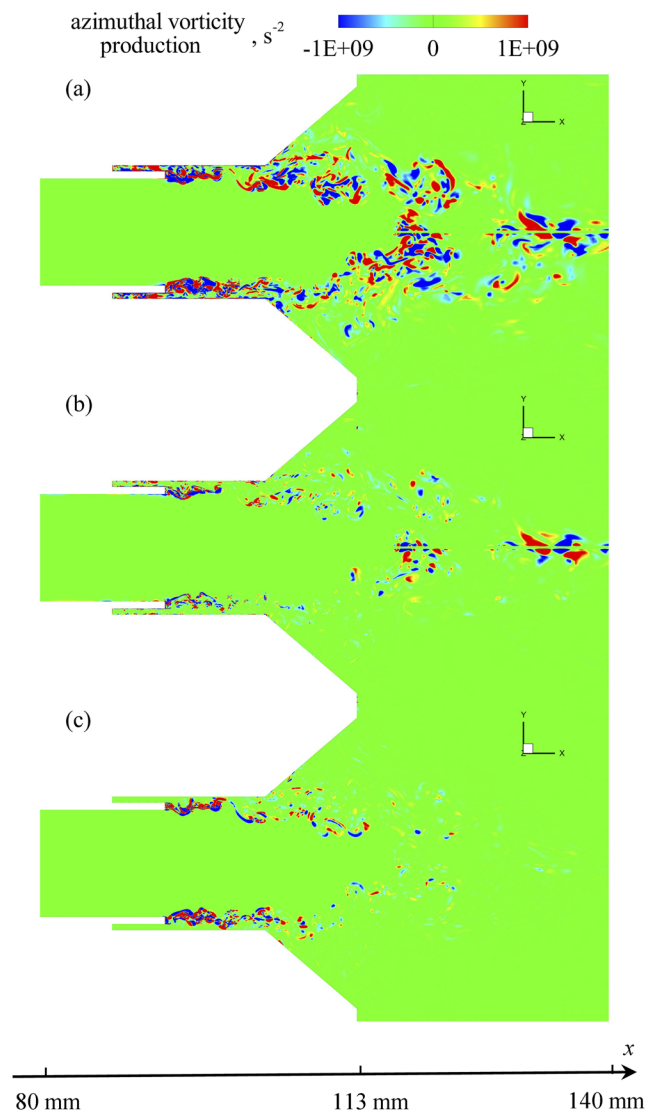
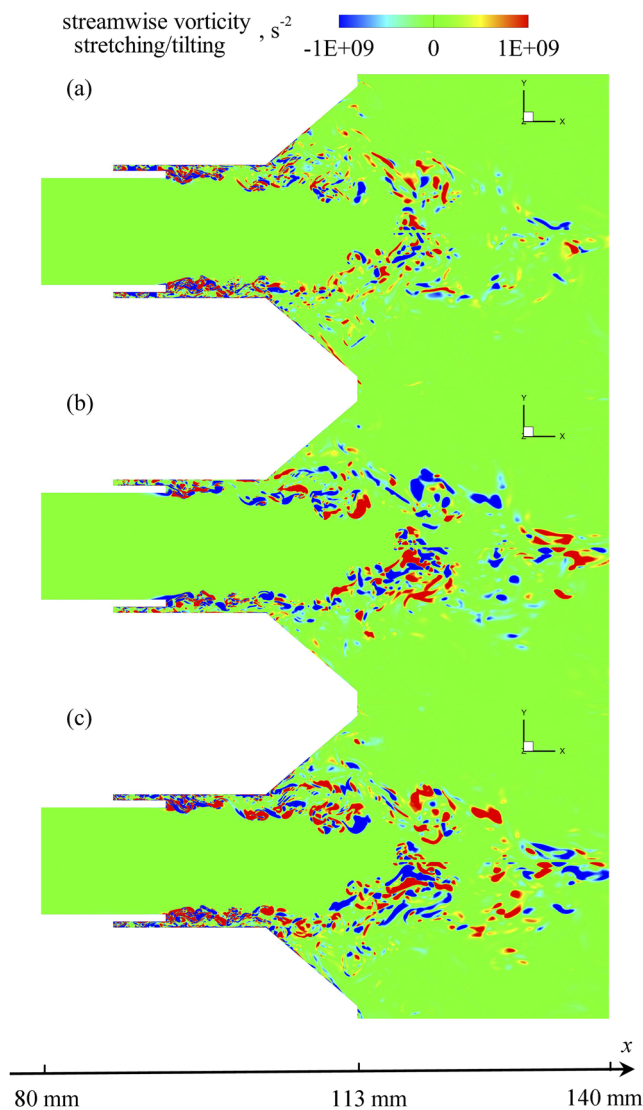


FIG. 13. Instantaneous distributions of azimuthal vorticity production terms: (a) vortex stretching/tilting, (b) volume dilatation, and (c) baroclinic torque on the  $z = 0$  plane.

thermal gradient and vortex interactions lead to volume dilatation and misalignment of density and pressure gradients in both the axial and radial directions (see Fig. 9), thereby generating additional azimuthal vorticity. These effects, combined with vortex stretching and tilting, result in positive azimuthal vorticity in the recess region (see Fig. 11). The production of azimuthal vorticity is more dynamic in the taper region due to radial expansion and flow recirculation.

The production mechanism of streamwise vorticity is crucial to the understanding of the origin of transverse instability. On the right-hand side of Eq. (6), the terms in the first bracket denote radial tilting, azimuthal tilting, and streamwise stretching, respectively. Figure 14 shows snapshots of these terms on the  $z = 0$  plane. They all play a significant role in vorticity production in the



**FIG. 14.** Instantaneous distributions of (a) streamwise stretching, (b) azimuthal tilting, and (c) radial tilting in strain-vorticity interactions in streamwise vorticity budget on the  $z = 0$  plane.

recess region. Downstream of the recess region, azimuthal tilting  $[(\omega_\theta/r)\partial u_x/\partial\theta]$  and radial tilting  $(\omega_r\partial u_x/\partial r)$  exert stronger influence, followed by the streamwise stretching. The azimuthal tilting results partially from the vorticity transfer in the azimuthal direction, where the intensity is strongest because of the radial expansion in the taper region, as indicated in Fig. 11. Another contributing factor is the velocity asymmetry in the azimuthal direction. As revealed in Fig. 10, the circumferential nonuniformity of the GOX stream produces a large axial velocity gradient in the azimuthal direction  $(\partial u_x/\partial\theta)$ . This manifests the critical role of the streamwise vorticity in the azimuthal instability. The effect of the radial tilting is primarily determined by the axial velocity gradient in the radial direction, the largest element in the velocity gradient tensor.

Figure 15 shows snapshots of vortex stretching/tilting, volume dilatation, and baroclinic torque on the  $z = 0$  plane. The effect of vortex stretching/tilting clearly dominates the vorticity production. Similar to the situation for azimuthal vorticity, volume dilatation and baroclinic torque are also present in the wake of the GOX post tip. Vortex stretching and tilting are the main cause of the Kelvin-Helmholtz (primary) shear-layer instability, while dilatational and baroclinic effects are responsible for secondary instabilities and the formation of lobes and ligaments circumferentially. This is consistent with observations from Figs. 6 and 7. The dilatational effect gradually decreases along the axial direction due to thermal and mass diffusion. The baroclinic effect shows the same trend.

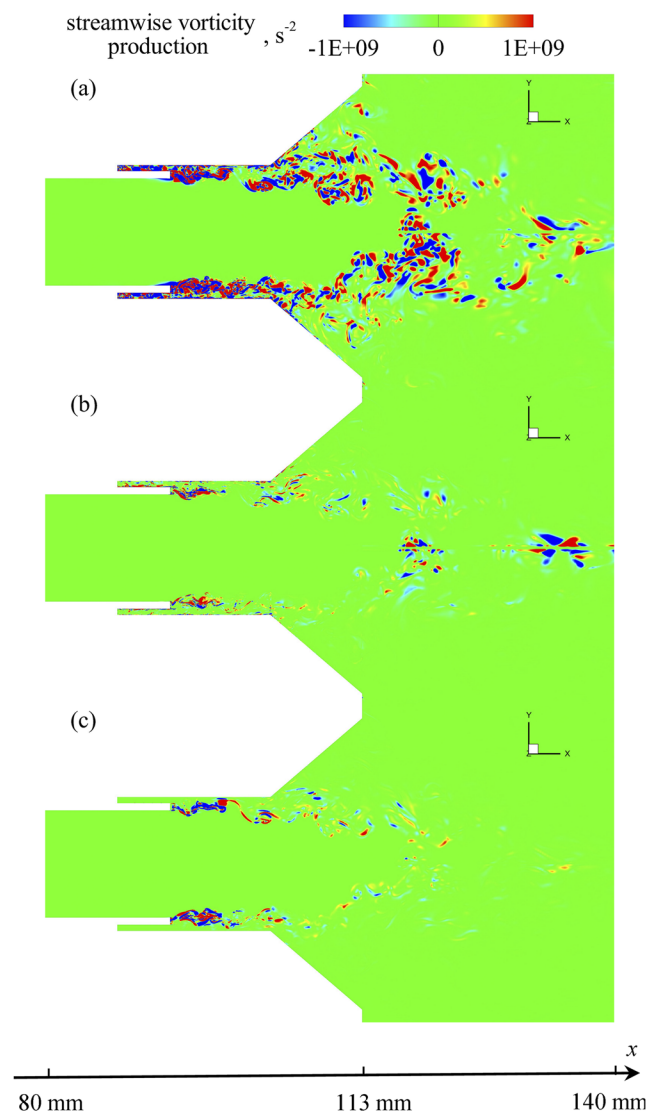


**FIG. 15.** Instantaneous distributions of streamwise vorticity production terms: (a) vortex stretching/tilting, (b) volume dilatation, and (c) baroclinic torque on the  $z = 0$  plane.

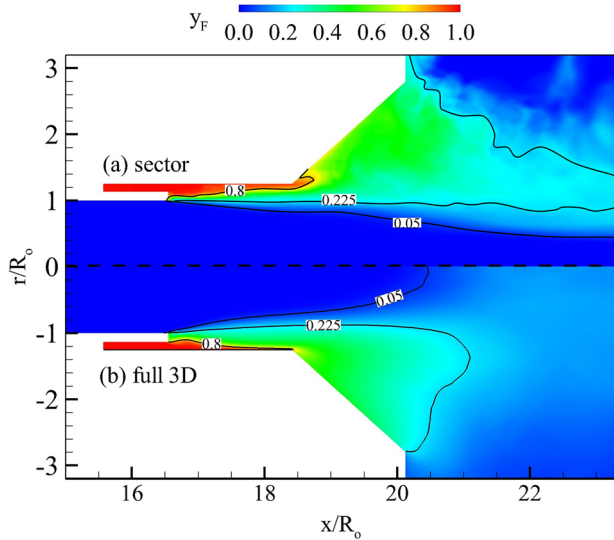


FIG. 16. Time-averaged kerosene mass fraction field in (bottom) full three-dimensional and (top) sector configurations.

C. Mean flowfield

Figure 16 shows the time-averaged distribution of kerosene mass fraction in the full three-dimensional and sector configurations, separated by the centerline. The results in the full three-dimensional case are further azimuthally averaged. Propellant mixing is underpredicted for the sector configuration. The iso-contour line of kerosene mass fraction of 0.8 penetrates to the taper region, while it disappears at the recess exit in the three-dimensional configuration. The central GOX stream, enclosed by the contour line of 0.05, flows all the way to the exit of the downstream domain for the sector configuration. The GOX core is, however, enclosed near the taper exit in the three-dimensional configuration. The mixedness of propellants is evidenced by the contour line of 0.225, i.e., the stoichiometric mixture ratio of GOX and kerosene. Complete stoichiometry is achieved at  $x/R_0 = 21$  in the three-dimensional configuration, but the stoichiometric line goes well beyond  $x/R_0 = 24$  in the sector configuration. As discussed earlier, the sector layout excludes azimuthal dynamics and secondary instabilities that are necessary for small-scale motions, leading to the underprediction of mixing.

Figure 17 presents time-averaged distributions of axial and azimuthal velocity components, kerosene mass fraction, and

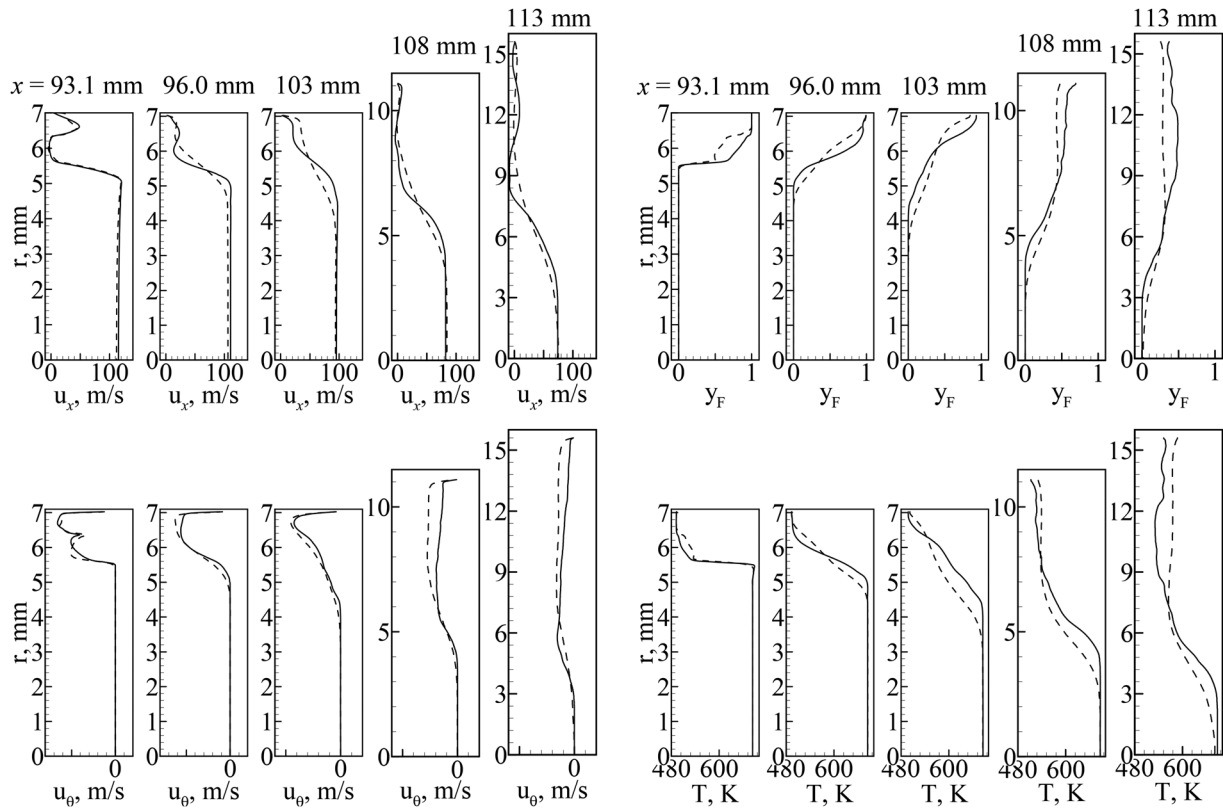


FIG. 17. Radial distributions of time-averaged axial and tangential velocities, kerosene mass fraction, and temperature at different locations for sector (solid lines) and three-dimensional (dashed lines) cases.

temperature in the radial direction at different axial locations for the two configurations. These locations span from the entrance of the recess region to the exit of the taper region. The two configurations show close agreement in the distributions of axial and azimuthal velocity components near the GOX post tip, implying similar shear-layer structures. The difference becomes evident further downstream of the post tip. In the three-dimensional configuration, the axial velocity profile tends to be smoother and the azimuthal velocity profile is fuller. In other words, the sector configuration predicts a higher axial velocity gradient and a smaller azimuthal velocity gradient in the radial direction. The maximum azimuthal velocity becomes significantly smaller in the taper region. Also shown in Fig. 17 are the profiles of kerosene mass fraction and temperature, which change more abruptly in the sector configuration and are consistent with that of axial velocity, resulting in underestimated species and thermal mixing.

Figure 18 shows the time-averaged distributions of kerosene mass fraction at different cross sections in the recess region for the three-dimensional configuration. The GOX core is initially circular, becomes hexagonal, and shrinks continuously along the axial direction as the propellant mixing proceeds. The formation of the hexagonal core is attributed to the interaction between the central GOX and coaxial kerosene streams. The process can be explained through the vorticity magnitude field in Fig. 19. At  $x = 93$  mm, a hexagonlike vortex ring forms and detaches from the coaxial annulus surface, while a circular vortex ring separates from the GOX post surface. When transported downstream, the two vortex rings merge and form a new ring. As a result, the new ring has nonuniformly distributed strength of vorticity, with a peak value on the hexagonal vertices. Such nonuniformity further develops as the vorticity magnitude on the edges further decreases in the downstream region. Six discrete vortex cores are thus generated, and they reside on the edges of the hexagonal jet core. The vortices weaken as they travel downstream.

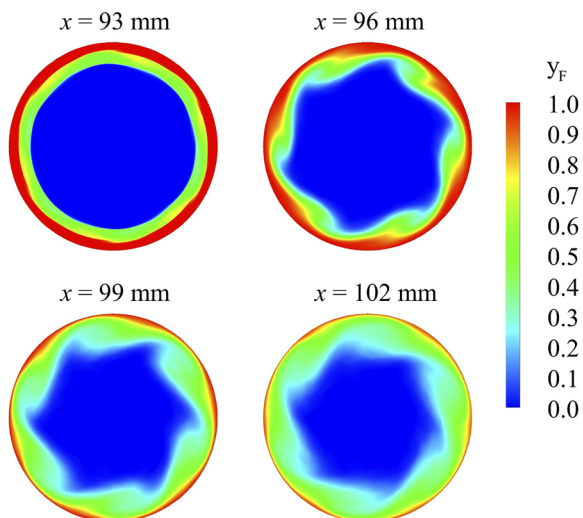


FIG. 18. Cross-sectional views of kerosene mass fraction field in the recess region.

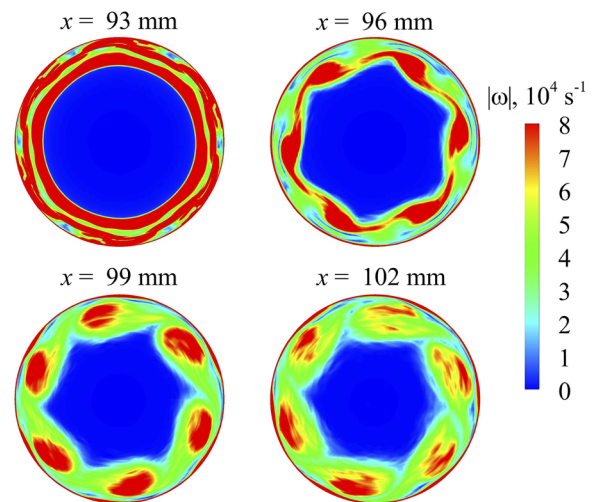


FIG. 19. Cross-sectional views of vorticity magnitude field in the recess region.

#### D. General mechanisms of flow instabilities

As shown schematically in Fig. 2, eight different types of flow structures and instability mechanisms are identified in the present GCLSC injector. First, the detached wall shear layers from the GOX post and coaxial annulus generate two small counter-rotating recirculation zones near the post tip. These two low-speed zones are crucial to stabilizing flames in the presence of combustion.<sup>13</sup> The detached shear layers interact and merge to form a new axial shear layer convecting downstream; as the shear layer moves downstream, the vortices roll up and grow into billows. In the meantime, the liquid film thickness fluctuates along both the axial and azimuthal directions because of the centrifugal instability induced by the oscillation of the swirl strength.

At the recess exit, the kerosene stream is largely entrained into the GOX stream, and flow separation and reattachment cause the fuel-rich mixture to divide into two branches entering the taper region. One branch reattaches to the taper surface, and the other is entrained by the central GOX stream. Radial expansion of the flow weakens the centrifugal force and pressure level along the surface. A positive pressure gradient in the axial direction arises, eventually leading to the formation of a recirculation zone near the taper surface.<sup>13</sup> Such flow evolution has at least two important consequences for the reacting flow. First, the fuel-rich mixture provides thermal protection to the taper surface from hot products. Second, the recirculation zone acts as a thermal pool to heat incoming reactants and stabilizes the combustion. The difference in azimuthal velocity in the radial direction leads to the formation of an azimuthal shear layer, on which secondary instabilities develop because of the misalignment of the density and pressure gradients (the Rayleigh-Taylor instability) and volume dilatation. The secondary instabilities significantly enhance small-scale mixing. The flow dynamics in the downstream region can induce pressure disturbance that propagates upstream to the GOX and kerosene inlets in the form of an acoustic wave. More in-depth analysis is needed to quantify the characteristic frequencies associated with flow instabilities, a subject for the future work.

## V. CONCLUSIONS

This paper presents a comprehensive computational study of three-dimensional flow dynamics in a gas-centered liquid-swirl coaxial injector at supercritical pressure. Turbulence closure is achieved using the large-eddy-simulation technique. Gaseous oxygen (GOX) is axially delivered into the center GOX post, and kerosene is tangentially introduced through discrete orifices on the surface of the coaxial annulus. The operating and geometric conditions are similar to those of the main injector element used in staged-combustion engines such as the RD170/180 engine.

The complex flow dynamics are discussed in detail. Various types of key flow structures and instability mechanisms are identified, including recirculation in the wake of the GOX post and underneath the taper, axial and azimuthal shear-layer instabilities, centrifugal instability, flow separation and reattachment at the entrance of taper, secondary instabilities, and acoustic waves. The roles of these mechanisms are explored in terms of vorticity transport in the streamwise and azimuthal directions. The axial and azimuthal velocity gradients promote shear-layer instabilities, on which secondary instabilities develop and significantly enhance small-scale mixing. Baroclinic torque and volume dilatation, responsible for the secondary instabilities, are prominent in the recess region. The GOX core displays a hexagonal shape due to the interactions of vortex rings detached from the center post and coaxial annulus. For comparison, a cylindrical sector of the configuration is also simulated. The result underpredicts the degree of propellant mixing in the recess and taper regions due to the absence of complete azimuthal dynamics and secondary instabilities.

## ACKNOWLEDGMENTS

This work was sponsored by the Air Force Office of Scientific Research under Grant No. FA 9550-18-1-0216. The authors gratefully acknowledge support and advice from Mitat A. Birkan.

## REFERENCES

- D. Manski, C. Goertz, H.-D. Saßnick, J. R. Hulka, B. D. Goracke, and D. J. H. Levack, "Cycles for Earth-to-orbit propulsion," *J. Propul. Power* **14**, 588 (1998).
- A. A. Vasin, S. D. Kamensky, B. I. Katargin, A. I. Kolesnikov, V. P. Nosov, A. I. Stavrulov, V. V. Fedorov, and V. K. Chvanov, "Liquid-propellant rocket engine chamber and its casing," U.S. patent 6,244,041 B1 (12 June 2001).
- M. L. Dranovsky, "Combustion instabilities in liquid rocket engines: Testing and development practices in Russia," in *Progress in Astronautics and Aeronautics*, edited by V. Yang, F. Culick, and D. G. Talley (AIAA, 2007), Vol. 221.
- V. Yang, D. Ku, C. Lioi, S.-T. Yeh, J. C. Leahy, and R. J. Kenny, "Liquid oxygen/kerosene oxygen-rich, staged combustion engine technology development," NASA/TP 2016-218226, 2016.
- C. Lioi, D. Ku, and V. Yang, "Linear acoustic analysis of main combustion chamber of an oxidizer-rich staged combustion engine," *J. Propul. Power* **34**, 1505 (2018).
- L.-J. Yang, M.-H. Ge, M.-Z. Zhang, Q.-F. Fu, and G.-B. Cai, "Spray characteristics of recessed gas-liquid coaxial swirl injector," *J. Propul. Power* **24**, 1332 (2008).
- V. Kulkarni, D. Sivakumar, C. Oommen, and T. Tharakan, "Liquid sheet breakup in gas-centered swirl coaxial atomizers," *J. Fluids Eng.* **132**, 011303 (2010).
- J. Jeon, M. Hong, Y.-M. Han, and S. Y. Lee, "Experimental study on spray characteristics of gas-centered swirl coaxial injectors," *J. Fluids Eng.* **133**, 121303 (2011).
- J.-P. Matas, M. Hong, and A. Cartellier, "Stability of a swirled liquid film entrained by a fast gas stream," *Phys. Fluids* **26**, 042108 (2014).
- H. C. Balance, O. Bibik, T. S. Cook, S. Danczyk, S. A. Schumaker, V. Yang, and T. C. Lieuwen, "Optical diagnostics in a high-pressure combustor with gaseous oxygen and kerosene," *J. Propul. Power* **35**, 13 (2018).
- M. E. Harvazinski, C. Huang, V. Sankaran, T. W. Feldman, W. E. Anderson, C. L. Merkle, and D. G. Talley, "Coupling between hydrodynamics, acoustics, and heat release in a self-excited unstable combustor," *Phys. Fluids* **27**, 045102 (2015).
- L. Zhang, X. Wang, Y. Li, S.-T. Yeh, and V. Yang, "Supercritical fluid flow dynamics and mixing in gas-centered liquid-swirl coaxial injectors," *Phys. Fluids* **30**, 075106 (2018).
- X. Wang, L. Zhang, Y. Li, S.-T. Yeh, and V. Yang, "Supercritical combustion of gas-centered liquid-swirl coaxial injectors for staged-combustion engines," *Combust. Flame* **197**, 204 (2018).
- W. O. H. Mayer, A. H. A. Schik, B. Vielle, C. Chauveau, I. Gokalp, D. G. Talley, and R. D. Woodward, "Atomization and breakup of cryogenic propellants under high-pressure subcritical and supercritical conditions," *J. Propul. Power* **14**, 835 (1998).
- S. Candel, M. Juniper, G. Singla, P. Scoufflaire, and C. Rolon, "Structure and dynamics of cryogenic flames at supercritical pressure," *Combust. Sci. Technol.* **178**, 161 (2006).
- K. Miller, J. Sisco, N. Nugent, and W. Anderson, "Combustion instability with a single-element swirl injector," *J. Propul. Power* **23**, 1102 (2007).
- J. G. Kim, Y. M. Han, H. S. Choi, and Y. Yoon, "Study on spray patterns of gas-centered swirl coaxial (GCSC) injectors in high pressure conditions," *Aerosp. Sci. Technol.* **27**, 171 (2013).
- C. Muthukumar and A. Vaidyanathan, "Initial instability of round liquid jet at subcritical and supercritical environments," *Phys. Fluids* **28**, 074104 (2016).
- S. DeSouza and C. Segal, "Sub-and supercritical jet disintegration," *Phys. Fluids* **29**, 047107 (2017).
- Y. Li, X. Wang, L. Zhang, and V. Yang, "A parametric study of gas-centered liquid-swirl coaxial injector flow dynamics at supercritical conditions," *Phys. Rev. Fluids* (submitted).
- V. Yang, "Modeling of supercritical vaporization, mixing, and combustion processes in liquid-fueled propulsion systems," *Proc. Combust. Inst.* **28**, 925 (2000).
- H. Huo and V. Yang, "Large-eddy simulation of supercritical combustion: Model validation against gaseous H<sub>2</sub>-O<sub>2</sub> injector," *J. Propul. Power* **33**, 1272 (2017).
- X. Wang, H. Huo, U. Unnikrishnan, and V. Yang, "A systematic approach to high-fidelity modeling and efficient simulation of supercritical fluid mixing and combustion," *Combust. Flame* **195**, 203 (2018).
- G. Soave, "Equilibrium constants from a modified Redlich-Kwong equation of state," *Chem. Eng. Sci.* **27**, 1197 (1972).
- H. Meng and V. Yang, "A unified treatment of general fluid thermodynamics and its application to a preconditioning scheme," *J. Comput. Phys.* **189**, 277 (2003).
- N. Zong and V. Yang, "An efficient preconditioning scheme for real-fluid mixtures using primitive pressure-temperature variables," *Int. J. Comput. Fluid Dyn.* **21**, 217 (2007).
- R. C. Swanson and E. Turkel, "On central-difference and upwind schemes," *J. Comput. Phys.* **101**, 292 (1992).
- X. Wang, "Swirling fluid mixing and combustion dynamics at supercritical conditions," Ph.D. thesis, Georgia Institute of Technology, 2016.
- H.-G. Li, P. Khare, H.-G. Sung, and V. Yang, "A large-eddy-simulation study of combustion dynamics of bluff-body stabilized flames," *Combust. Sci. Technol.* **188**, 924 (2016).
- H. G. Li, N. Zong, X. Y. Lu, and V. Yang, "A consistent characteristic boundary condition for general fluid mixture and its implementation in a preconditioning scheme," *Adv. Appl. Math. Mech.* **4**, 72 (2012).

<sup>31</sup>D. J. Bodony, “Analysis of sponge zones for computational fluid mechanics,” *J. Comput. Phys.* **212**, 681 (2006).

<sup>32</sup>V. Bazarov, V. Yang, and P. Puri, “Design and dynamics of jet and swirl injectors,” in *Liquid Rocket Thrust Chambers: Aspects of Modeling, Analysis, and Design*, Progress in Astronautics and Aeronautics Vol. 200 (AIAA, 2004), p. 19.

<sup>33</sup>D. Jarrabhshi and W. Sirignano, “Vorticity dynamics for transient high-pressure liquid injection,” *Phys. Fluids* **26**, 101304 (2014).

<sup>34</sup>J.-Z. Wu, H.-Y. Ma, and M.-D. Zhou, *Vorticity and Vortex Dynamics* (Springer Science & Business Media, 2007).

<sup>35</sup>G. Brown and J. Lopez, “Axisymmetric vortex breakdown Part 2. Physical mechanisms,” *J. Fluid Mech.* **221**, 553 (1990).